Robust Red Organic Nanoparticles for In Vivo Fluorescence Imaging of Cancer Cell Progression in Xenografted Zebrafish

Gengwei Lin, Purnima Naresh Manghnani, Duo Mao, Cathleen Teh, Yinghao Li, Zujin Zhao, Bin Liu,* and Ben Zhong Tang**

Bright and red-emissive organic nanoparticles (NPs) are demonstrated as promising for in vivo fluorescence imaging. However, most red organic dyes show greatly weakened or quenched emission in the aggregated state. In this work, a robust red fluorophore (*t*-BPITBT-TPE) with strong aggregate-state photoluminescence and good biocompatibility is presented. The NPs comprised of *t*-BPITBT-TPE aggregates encapsulated within 1,2-distearoyl-*sn*-glycero-3-phosphoethanolamine-*N*-[methoxy(polyethylene glycol) (DSPE-mPEG) micelles exhibit a photoluminescence peak at 660 nm with a high fluorescence quantum yield of 32% in aqueous media. The NPs can be facilely charged by using the same polymeric matrix with different terminal groups, e.g., methoxy (DSPE-mPEG), amine (DSPE-PEG-NH_2), or carboxymethyl (DSPE-PEG-COOH) groups. The biocompatibility, toxicity, circulation, and biodistribution of the NPs are assessed using the zebrafish model through whole embryo soaking and intravenous delivery. Furthermore, HeLa and MCF-7 cells tagged with *t*-BPITBT-TPE in DSPE-PEG-NH_2-TAT polymer NPs are xenografted into zebrafish larvae to successfully track the cancer cell proliferation and metastasis, demonstrating that these new NPs are efficient cancer cell trackers. In addition, the NPs also show good in vivo imaging ability toward 4T1 tumors in xenografted BALB/c mice.

1. Introduction

Noninvasive live animal fluorescence imaging has emerged as a promising technique to provide valuable in vivo information for disease diagnosis and therapy.[1] The quality and resolution of fluorescence imaging is highly dependent on the contrast agents for which strong photoluminescence (PL), high photostability, good biocompatibility, and excellent physical stability are desirable properties.[1b,2] Fluorescent organic nanoparticles (NPs) built with emissive organic aggregates and biocompatible polymeric matrices enjoy lower cytotoxicity and higher structural variety relative to inorganic quantum dots.[3] They also have better photostability than fluorescent proteins[4] and small-molecule dyes.[5] Through selection or modification of the polymeric matrices, emissive organic NPs with excellent properties, such as good water dispersibility and stability, feasible surface charge regulation, high target selectivity, and other designated functionalities, can be facilely realized.[3b,6] Therefore, they are considered to be excellent labeling reagents for fluorescence bioimaging applications.

The light-emissive molecules determine the optical property of organic NPs. In comparison with other visible light-emitting fluorophores, red fluorescent molecules are more desirable in fluorescence imaging applications because of their minimized autofluorescence interference, lowered damage to living cells, and increased penetration depth.[1a,7] In order to construct red organic fluorophores, extended π-conjugation and/or electronic donor–acceptor (D–A) structures with strong dipole moments are generally involved in the molecular design.[8] However, the large and planar π-conjugated system often results in strong π–π stacking interactions between molecules, while D–A structures can also lead to serious intermolecular dipole–dipole interactions. Both processes can increase the nonradiative decay rate, leading to decreased fluorescence quantum yield (Φ_F) in the aggregated state.[7b,8b,c] Therefore, many red fluorescent molecules suffer from aggregation-caused quenching, which is an obstacle in their practical applications. In this regard, luminescent materials with aggregation-induced emission (AIE) attributes have shown great potentials in bioimaging applications due to their intensified emission in the aggregated state.[9] Based on the understanding of AIE mechanism, diverse new luminogens with AIE characteristics (AIEgens) have been developed over the past decade.[6a,10] The integration of AIE-active units and

G. Lin, Y. Li, Prof. Z. Zhao, Prof. B. Z. Tang
State Key Laboratory of Luminescent Materials and Devices
South China University of Technology
Guangzhou 510640, China
E-mail: mszjzhao@scut.edu.cn; tangbenz@ust.hk
P. N. Manghnani, Dr. D. Mao, Prof. B. Liu
Department of Chemical and Biomolecular Engineering
National University of Singapore
4 Engineering Drive 4, Singapore 117585, Singapore
E-mail: cheliub@nus.edu.sg
Dr. C. Teh
Institute of Molecular and Cell Biology
Biopolis, Singapore 138673, Singapore
Prof. B. Z. Tang
Department of Chemistry
Hong Kong Branch of Chinese National Engineering
Research Center for Tissue Restoration and Reconstruction
The Hong Kong University of Science and Technology
Clear Water Bay, Kowloon, Hong Kong, China

DOI: 10.1002/adfm.201701418

other functional moieties has been rationalized to be a straightforward strategy to create efficient aggregate-state luminescent materials, and has furnished numerous bright fluorescent contrast agents for sensing, imaging, and therapy applications.[11]

Among the various animal models used to evaluate these NPs, zebrafish is an attractive model for toxicity, biocompatibility, biodistribution, immune response, teratogenicity, and long-term effect studies.[12] Zebrafish is a vertebrate model whose 99% embryonic essential genes are conserved in humans.[13] The ease of obtaining zebrafish embryos from fertile adults, the small embryo size, and their optical transparency make it a compatible model for assessment of fluorescent dyes using standard imaging microscope.[14] Novel fluorescent dyes can be assessed for desirable properties such as photostability and brightness of fluorescent signals detected through living tissues during whole embryo imaging.[15] In addition, as human oncogenes and tumor suppressor genes have homologs in zebrafish, many neoplastic signaling pathways between humans and zebrafish are conserved.[16] Zebrafish model is hence ideal for monitoring of in vivo tumor growth, angiogenesis, and metastasis.[17] What is of particular significance is that zebrafish larvae have immature adaptive immune system until one month post-fertilization.[18] As a result, human cancer cells can survive and metastasize in zebrafish.[19]

In this contribution, we report two efficient red fluorophores PITBT-TPE and *t*-BPITBT-TPE with a D–A structure (**Scheme 1**), in which benzothiadiazole segment serves as electron-withdrawing moiety (A), while 1-phenyl-2-(thiophen-2-yl)-1*H*-phenanthro[9,10-*d*]imidazole segment functions as electron-donating moiety (D). Considering that strong D–A interactions often decrease the Φ_F value in the aggregated state, tetraphenylethene (TPE), a typical AIE-active unit, is incorporated to yield PITBT-TPE. As the 9,10-phenanthroimidazole fragment is a large flat structure, a bulky *tert*-butyl group is further introduced into PITBT-TPE to minimize the π–π interaction and form a new red fluorophore of *t*-BPITBT-TPE. *t*-BPITBT-TPE was further encapsulated into polymeric micelles with different surface charges to form organic NPs stable in aqueous media. The generated NPs were used to analyze the behavior of *t*-BPITBT-TPE and the surface charge from different polymeric encapsulating matrices, DSPE-mPEG, DSPE-PEG-NH_2, DSPE-PEG-COOH, and DSPE-PEG-NH_2-TAT on the health of zebrafish larvae and the circulation of NPs in zebrafish. The toxicity, biodistribution and degradation of the different NPs were analyzed in the zebrafish larvae through transdermal and intravenous delivery. Furthermore, highly invasive metastatic cervical cancer cells (HeLa) and nonmetastatic breast cancer cells (MCF-7) were tagged with the *t*-BPITBT-TPE fluorescent NPs and were xenografted into the zebrafish yolk sac to track for cancer cell proliferation and metastasis over 5 d. The duration of assessment was limited to a week as development and activation of the immune response would lead to tumor cell death or xenograft lethality.[20] Finally, the fluorescence imaging ability of NPs toward 4T1 tumors in xenografted BALB/c mice was evaluated and the NP distribution in the major organs of mice was studied.

2. Results and Discussion

The synthetic approaches toward PITBT-TPE and *t*-BPITBT-TPE are illustrated in **Scheme 2**. PITBT-TPE and *t*-BPITBT-TPE were obtained through Suzuki reaction between the intermediate **4** or **5** and **6** using $Pd(PPh_3)_4$ as the catalyst, where **4**[21] and **5**[22] were prepared according to the synthetic processes published previously. The detailed synthesis and characterization results for both are provided in the Experimental Section.

The single crystals of both PITBT-TPE and *t*-BPITBT-TPE were obtained for structure analysis. They were grown from dichloromethane/methanol and dichloromethane/ethanol mixtures, respectively, and analyzed by X-ray diffraction crystallography. As depicted in **Figure 1**, the TPE moiety in PITBT-TPE adopts a twisted conformation to prevent π–π stacking interactions, but the 2,1,3-benzothiadiazole (BT), thiophene (Th) and 9,10-phenanthroimidazole (PI) fragments are aligned almost in the same plane, which is in favor of π–π stacking interactions in the aggregated state. The torsion angles between BT, Th, and PI are only 1.42° and 3.11°, respectively. However, they are increased to 3.85° and 9.37°, respectively, in *t*-BPITBT-TPE. The more twisted conformation can alleviate the intermolecular π–π stacking interactions to some degree. Due to the incorporation of *tert*-butyl, the molecular packing pattern of *t*-BPITBT-TPE differs from that of PITBT-TPE (**Figure 2**A). The crystal structures of PITBT-TPE and *t*-BPITBT-TPE belong to monoclinic and triclinic crystal systems, respectively. Figure 2B illustrates the position relationship of PITBT-TPE or *t*-BPITBT-TPE molecule with two face-to-face adjacent molecules in the crystals. As for PITBT-TPE, the BT and Th fragments are partially face-to-face with the Th and BT fragments of one of the adjacent molecules, respectively. The shortest distance from Th ring to the plane of BT of the adjacent molecule is 3.43 Å, indicative of π–π stacking interaction between the molecules. The BT and Th fragments are also faced to the PI fragment of the other

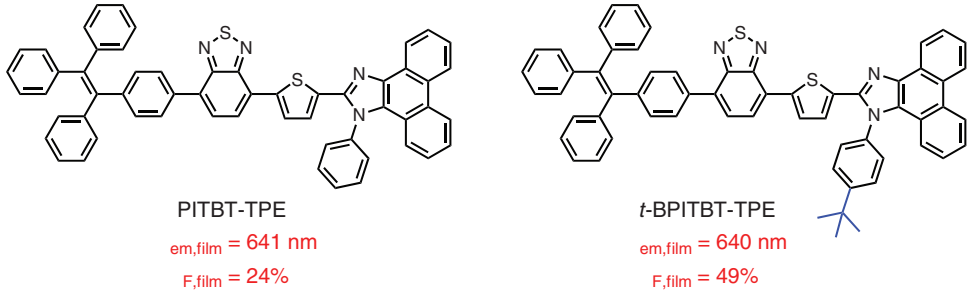

Scheme 1. Chemical structures of PITBT-TPE and *t*-BPITBT-TPE.

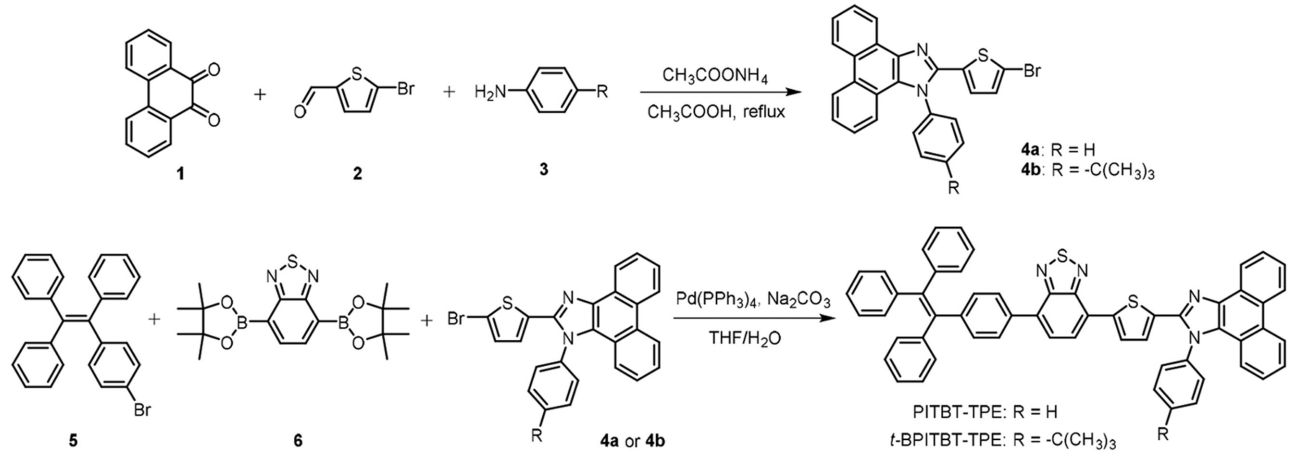

Scheme 2. Synthetic routes to PITBT-TPE and *t*-BPITBT-TPE.

adjacent molecule in part, with the shortest distance of 3.42 and 3.31 Å from BT and Th to the PI plane. All the distances indicated in Figure 2B suggest the existence of π–π stacking interactions between adjacent PITBT-TPE molecules. However, the face-to-face interactions are significantly weakened in adjacent *t*-BPITBT-TPE molecules, which are witnessed by the diminished interaction area between BT and Th, and the increased distance between Th and the PI plane to 3.41 Å. These results demonstrate that as compared to PITBT-TPE, the π–π stacking interactions between *t*-BPITBT-TPE molecules are substantially weakened, which should favor improved emission efficiency in the aggregated state for the latter.

PITBT-TPE and *t*-BPITBT-TPE exhibit strong absorption maxima at 476 and 477 nm, respectively, in THF solution (10×10^{-6} M) with a molar absorptivity close to 3×10^4 M^{-1} cm^{-1} (**Figure 3**A). The molecularly dispersed PITBT-TPE in dilute THF solution shows intense PL peaking at 598 nm, with a high Φ_F value of 84%. *t*-BPITBT-TPE exhibits similar absorption, PL and Φ_F in dilute THF solution (Figure 3; **Table 1**), indicating that the incorporation of *tert*-butyl exerts little impact on the photophysical property of a dispersed molecule. This finding is consistent with the computational results as PITBT-TPE and *t*-BPITBT-TPE possess almost the same molecular conformations and identical spatial distributions of the lowest unoccupied molecular orbitals and the highest occupied molecular orbitals (Figure S1, Supporting Information). Due to the strong D–A interaction, *t*-BPITBT-TPE also shows strong solvatochromic effect (Figure S2, Supporting Information). The PL maximum of *t*-BPITBT-TPE in nonpolar cyclohexane is 559 nm, which is significantly red-shifted to 623 nm in polar *N*,*N*-dimethylformamide. The AIE property of *t*-BPITBT-TPE was studied in dimethyl sulfoxide (DMSO)–ethanol mixtures as an example (Figure S3, Supporting Information). As the ethanol content was increased, a poor solvent of *t*-BPITBT-TPE, the *t*-BPITBT-TPE molecules start to form aggregate, and the PL intensity of *t*-BPITBT-TPE is enhanced gradually, thanks to the AIE effect of TPE unit. But when the ethanol content is too high (>70 vol%), the PL intensity becomes lowered slightly, due to the strong dipole–dipole interactions in the highly condensed phase. In films, because of the strong π–π stacking interactions between PITBT-TPE molecules, the PL maximum of PITBT-TPE is red-shifted to 641 nm and the Φ_F is reduced to 24%. On the other hand, *t*-BPITBT-TPE has a PL maximum at 640 nm with a higher Φ_F of 49% in films. Although the Φ_F value of *t*-BPITBT-TPE in film is lower than that in THF solution, the AIE effect of TPE unit indeed offsets the emission quenching of dipole-dipole interactions, and the bulky *tert*-butyl group also efficiently mitigates the intermolecular π–π stacking interactions in the condensed phase to ensure a high Φ_F value.

To further understand the difference in PL behaviors, we measured the time-resolved fluorescence spectra of PITBT-TPE and *t*-BPITBT-TPE (Figure S4, Supporting Information) under ambient conditions. Their fluorescence lifetimes as well as calculated radiative and nonradiative decay rates are summarized in Table 1. Both PITBT-TPE and *t*-BPITBT-TPE show almost the same fluorescence lifetimes and radiative and nonradiative decay rates in THF, which is consistent with their PL results in

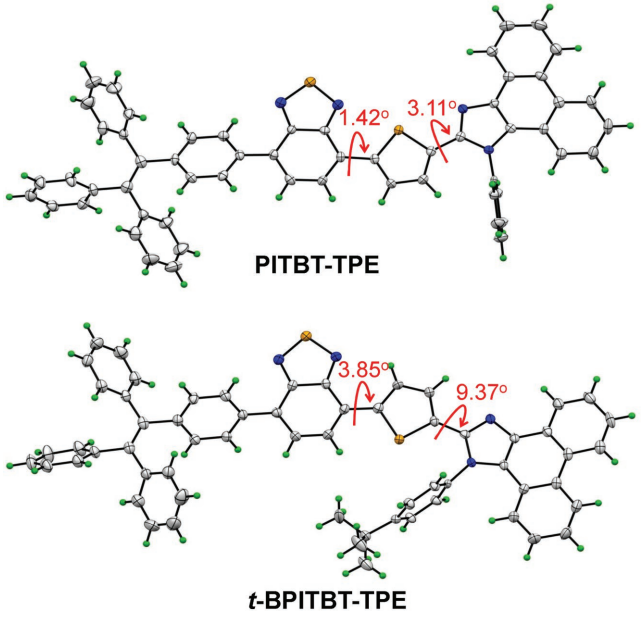

Figure 1. Crystal structures of PITBT-TPE (CCDC 1502965) and *t*-BPITBT-TPE (CCDC 1502964).

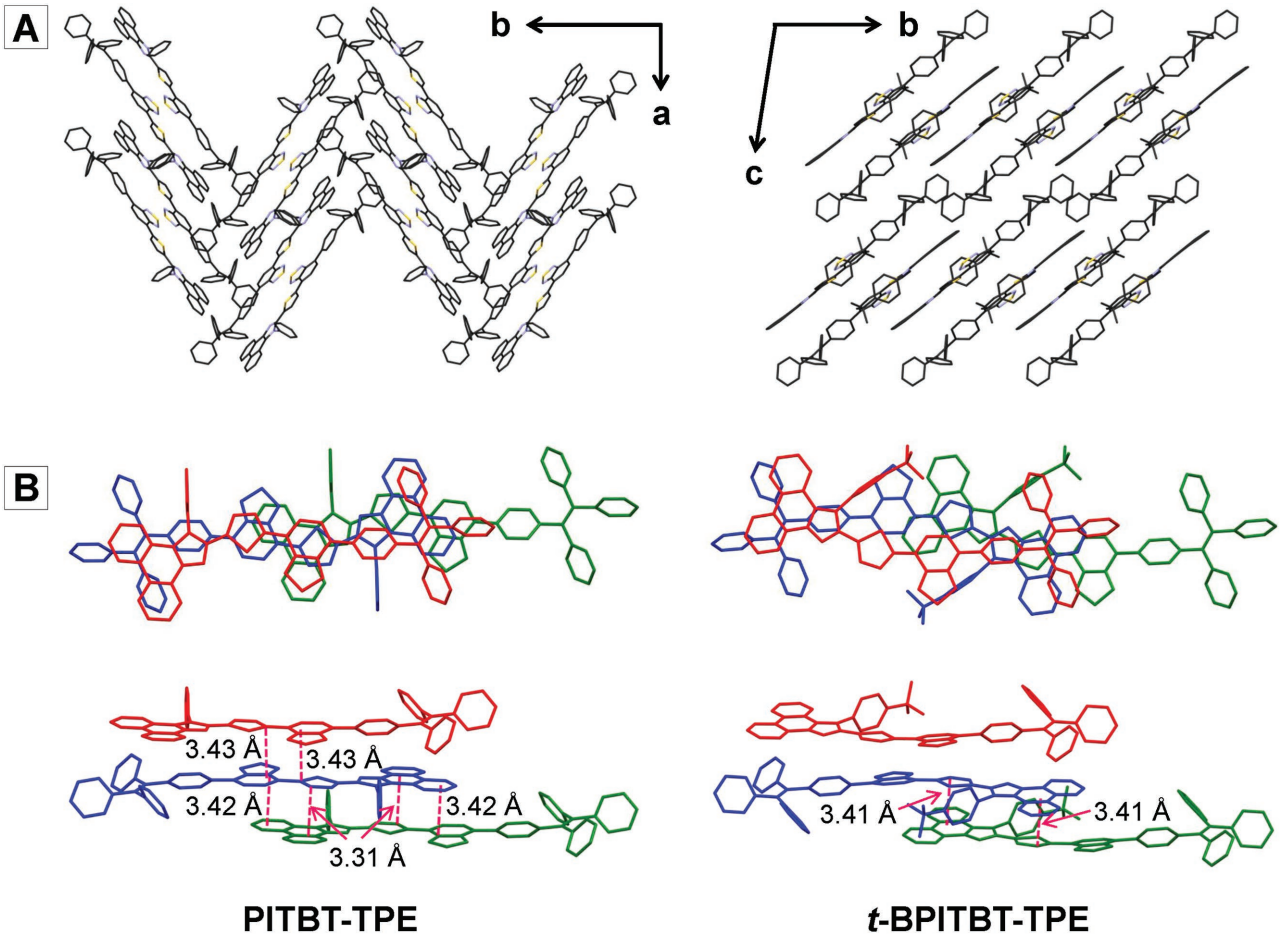

Figure 2. Illustration of A) crystal packing and B) intermolecular π–π stacking interactions of PITBT-TPE and *t*-BPITBT-TPE. The solvent molecules and hydrogen atoms are omitted for clarity.

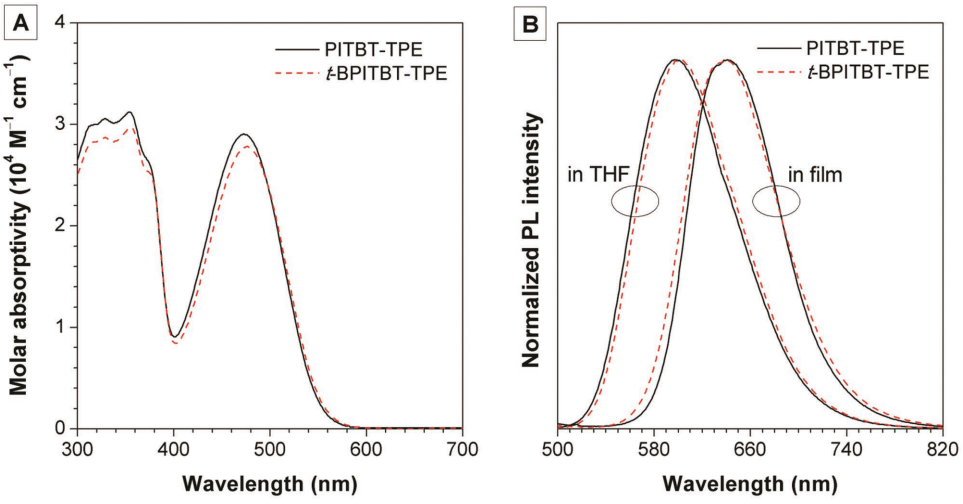

Figure 3. A) Absorption spectra in THF solutions and B) normalized photoluminescence spectra in THF solutions and films of PITBT-TPE and *t*-BPITBT-TPE.

Table 1. Photophysical properties of PITBT-TPE and *t*-BPITBT-TPE.

Compound	λ_{abs}[a] [nm]	λ_{em} [nm]		Φ_F[c] [%]		τ [ns]		k_r[d] [10^7 s^{-1}]		k_{nr}[e] [10^7 s^{-1}]	
		THF	Film[b]	THF	Film[b]	THF	Film[b]	THF	Film[b]	THF	Film[b]
PITBT-TPE	476	598	641	84	24	5.64	4.99	14.9	4.81	2.84	15.2
t-BPITBT-TPE	477	600	640	84	49	5.65	5.09	14.9	9.63	2.83	10.0

[a]Measured in THF (10×10^{-6} M); [b]Spin-coated film; [c]Absolute fluorescence quantum yield determined by a calibrated integrating sphere; [d]$k_r = \Phi_F/\tau$; [e]$k_{nr} = (1 - \Phi_F)/\tau$.

THF. For both molecules, the radiative decay rates (k_r) in films are lower than those in THF, while the nonradiative decay rates (k_{nr}) are higher, resulting in decreased Φ_F values in films. As compared to PITBT-TPE, *t*-BPITBT-TPE has a smaller k_{nr} but an approximately twice larger k_r in films, giving rise to its greatly increased Φ_F in the film state. The red PL and high solid-state Φ_F value make *t*-BPITBT-TPE a more promising fluorophore for fluorescence imaging.

To improve the water dispersibility of *t*-BPITBT-TPE for bioapplications, fluorescent NPs were fabricated by encapsulating the hydrophobic *t*-BPITBT-TPE in polymeric micelles via nanoprecipitation following the reported technique.[23] 1,2-Distearoyl-*sn*-glycero-3-phosphoethanolamine-*N*-[methoxy(polyethylene glycol) (DSPE-PEG$_{2000}$) block copolymers bearing hydrophobic and hydrophilic domains with different terminal functional groups allow spontaneous formation of micelles in aqueous media. This yields NPs born with methoxy (DSPE-mPEG), amine (DSPE-PEG-NH_2), or carboxymethyl (DSPE-PEG-COOH) groups (**Scheme 3**). Each surface modification generates different charges, thereby altering the behavior of the NPs. It has been shown that the amine groups impart positive charges and the carboxylic acid and methoxy groups impart negative charges to the uncharged PEG surface.[24] The cell penetrating peptide TAT, when conjugated to the surface of NPs, can alter the surface charge to positive value.[25]

All the NPs were subjected to size measurement using dynamic light scattering (DLS). The NPs have sizes of around 30 nm with a polydispersity index of less than 0.2, confirming the uniformity of the NPs produced (**Figure 4**A). The spherical nanoparticle morphology was also confirmed by using TEM (Figure S5, Supporting Information). The optical properties of the NPs, such as absorption and PL spectra, were found to be similar to each other and not significantly affected by the matrix. They show absorption and emission maxima at about 480 and 660 nm (Figure 4B), with a high Φ_F value of ≈32% in water relative to 4-(dicyanomethylene)-2-methyl-6-[4-(dimethylaminostyryl)-4H-pyran] (Φ_F = 43% in methanol). As expected, the carboxyl and methoxy groups impart negative charges to the NPs, resulting in net surface charge values of −45.82 ± 2.48 and −32.97 ± 0.9 mV, respectively. The amine group imparts a relatively positive charge to yield a net surface charge value of −20.78 ± 2.22 mV.

The initial toxicity response of wild-type zebrafish to the different surface properties of NPs was assessed using whole larvae soaking. The zebrafish embryos were collected after crossing the wild type parents and incubating the embryos in egg water with 1-phenyl-2-thiourea (PTU) at 28.5 °C and 0.4% CO_2 for 3 d. The biocompatibility of the different NPs was assessed by soaking the larvae 4 days postfertilization (dpf) with the NPs at different concentrations for 24 h (**Figure 5**B). The methodology further estimates the initial safe working dose for each type of NPs.

Based on the initial toxicity evaluation, a TAT peptide was further conjugated to the surface of DSPE-PEG-NH_2 NPs since they exhibited the least toxicity to zebrafish larvae. To facilitate

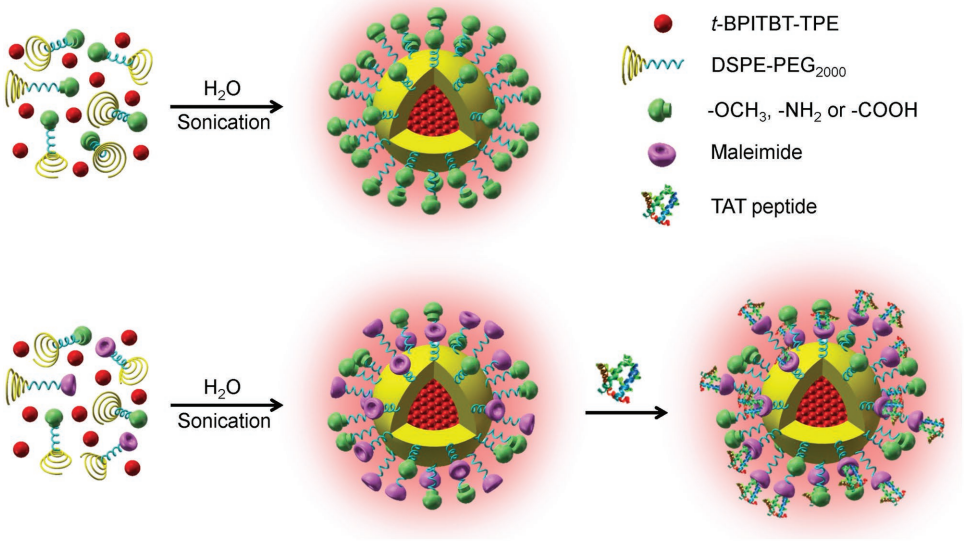

Scheme 3. Schematic illustration of the nanoprecipitation of *t*-BPITBT-TPE using DSPE-PEG block copolymers as the encapsulation matrices.

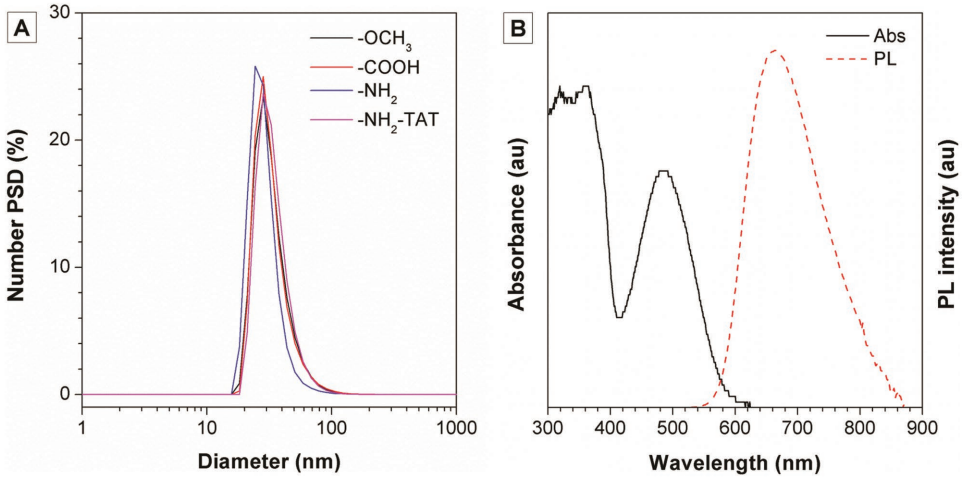

Figure 4. A) DLS measurements for the different NPs. B) Representative absorption and PL spectra of the NPs.

easy conjugation, a mixture of DSPE-PEG-NH_2 and DSPE-PEG-maleimide were used for the NP formation, which was followed by click reaction between a thiol functionalized TAT peptide and the surface maleimide group (Scheme 3). The TAT conjugation yielded NPs with a net positive surface charge value of 27 ± 0.65 mV and a hydrodynamic size of 30 nm. All the NPs were purified and concentrated by centrifugation filtration to yield a final NP stock at a concentration of 640 μg mL^{-1} based on *t*-BPITBT-TPE.

The NPs with NH_2 and NH_2-TAT surface functionalization were found to be nontoxic at the highest dose of 320 μg mL^{-1} (Figure 5B). The zebrafish larvae show no adverse side effects and continue to grow post treatment. However, the larvae upon treatment with the negatively charged NPs, i.e., with −COOH and $-OCH_3$ surface groups, show poor survival at the dose of 320 μg mL^{-1} (Figure 5A). As the concentration of these NPs is sequentially reduced, the survival improves. Since the core of the NPs is the same, the toxic response to the different NPs can be attributed to the different polymeric matrices. The polymeric shell surrounding the dye aggregate determines the net surface charge of the NPs and the increased toxicity of −COOH and $-OCH_3$ should be attributed to the relatively higher negative surface charges. This shows that the surface functionalization of the NPs carrying *t*-BPITBT-TPE aggregates affects the initial particle behavior and toxicity.

The healthy zebrafish larvae after soaking were imaged to characterize the uptake. The images revealed low uptake through the skin for all the negatively charged NPs. In the case of COOH and OCH_3 functionalization, due to their toxicity at high concentrations, the larvae incubated with 80 μg mL^{-1} of NPs were imaged to show undetectable fluorescence. Upon incubation with 320 μg mL^{-1} of the NH_2 functionalized NPs, the larvae failed to show any significant uptake through the skin due to the net negative surface charge, which is electrostatistically repelled by the negatively charged cell membrane. However, for the NH_2-TAT NPs (320 μg mL^{-1}), they were taken up through the skin after 24 h of soaking. This substantiates

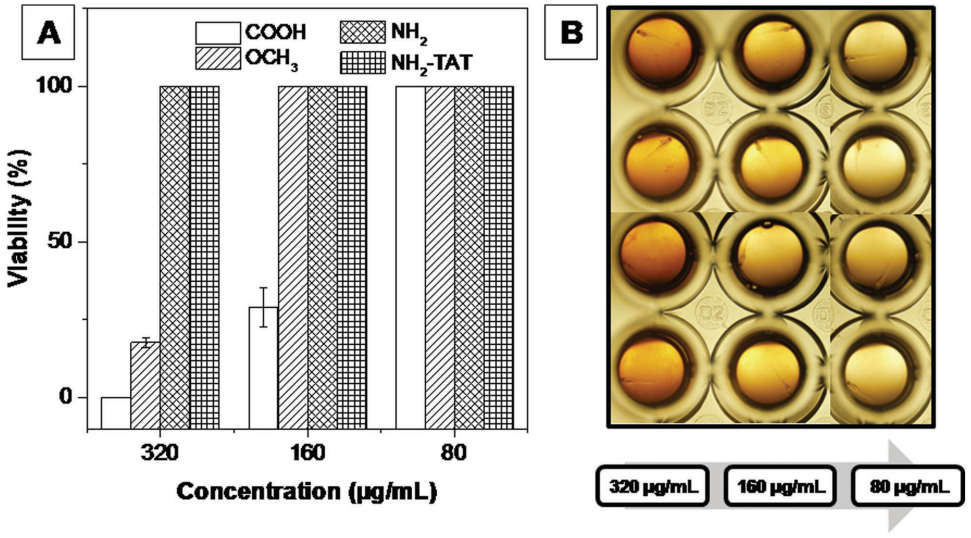

Figure 5. A) Percentage of embryo survival for whole embryo soaking in 320, 160, and 80 μg mL^{-1} NPs based on *t*-BPITBT-TPE concentration ($n = 17$). B) Sequential dilution of stock starting at 320 μg mL^{-1} *t*-BPITBT-TPE for NH_2-TAT NPs.

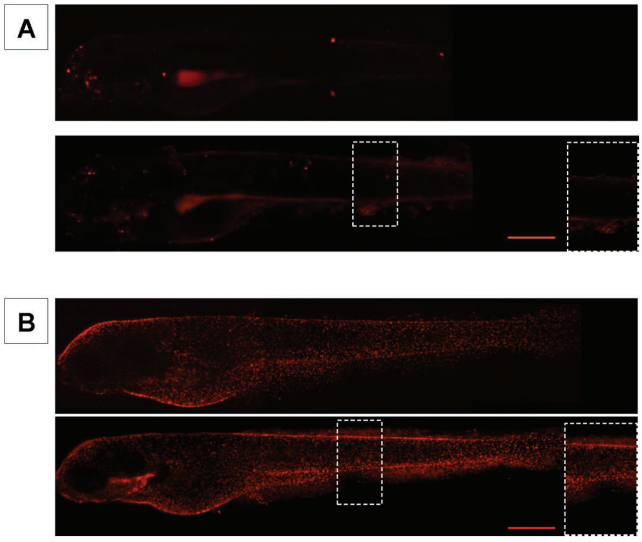

Figure 6. Confocal images of larvae showing normal development post 24 h of whole larval soaking with A) the NH_2 NPs and B) the NH_2-TAT NPs. The scale bar is 200 µm.

the claim that TAT loaded NPs have faster uptake due to better electrostatic interaction and enhanced cell-penetrating capability (**Figure 6**).

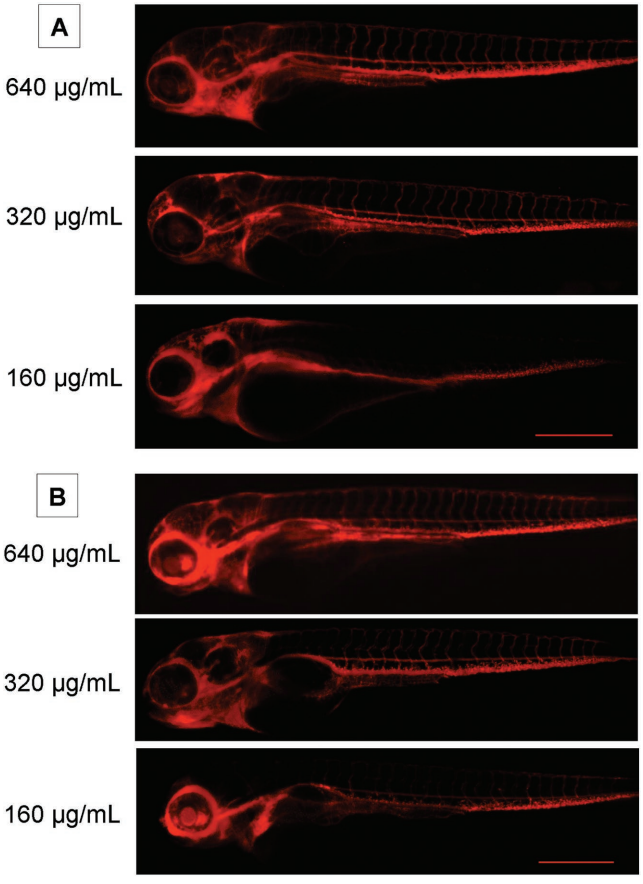

Figure 7. Embryos postinjection of A) NH_2 NPs and B) NH_2-TAT NPs at 640, 320, and 160 µg mL^{-1} based on *t*-BPITBT-TPE concentration. The scale bar is 200 µm.

Additional long-term toxicity evaluation was performed for the NH_2 and NH_2-TAT NPs since they showed most promising biocompatibility through soaking. Both NPs were injected separately and intravenously into 5 dpf wild type larvae retro-orbitally. The intravenous retro-orbital injection was performed using pneumatic microinjection in continuous mode. The larvae were injected with NPs at 640, 320, and 160 µg mL^{-1} based on *t*-BPITBT-TPE concentration to observe the intensity change with concentration. The maximum viable dose for intravenous injection is higher than that observed in whole larva soaking since intravenously injected dose is distributed throughout systemic circulation which is more benign than continuous exposure in the whole embryo soaking approach. The larvae were imaged postinjection with various concentrations of NPs and a clear difference in intensity was observed mainly in the circulation and in the trunk region (**Figure 7**).

To understand biodistribution of the NPs, both NH_2 and NH_2-TAT NPs (320 µg mL^{-1}) were injected separately to the embryos and the fluorescence was tracked for up to 7 d. It was found that the zebrafish larvae were healthy and did not develop any edema or cardiotoxicity. Although some of the NPs were in circulation for up to 2 d but most were taken up by cells in the first day itself. The difference in NP uptake was clearly discernable in the trunk region of the larva. The fluorescent signal in the trunk for the NH_2 NPs shows distribution and uptake through the tissue, and some of the NPs permeate through to the skin as well (**Figure 8**A). This suggests that the NPs permeate from the vasculature and are taken up unbiasedly. On

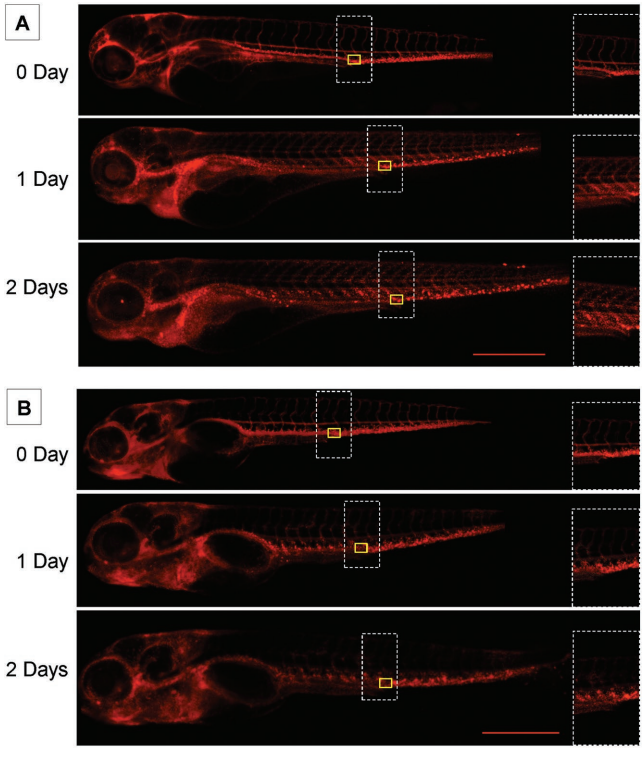

Figure 8. Embryos with A) NH_2 NPs and B) NH_2-TAT NPs at 320 µg mL^{-1} based on the *t*-BPITBT-TPE concentration postinjection, 1 d after injection and 2 d after injection. Dashed box is demarcating the caudal vein tissue and the scale bar is 200 µm.

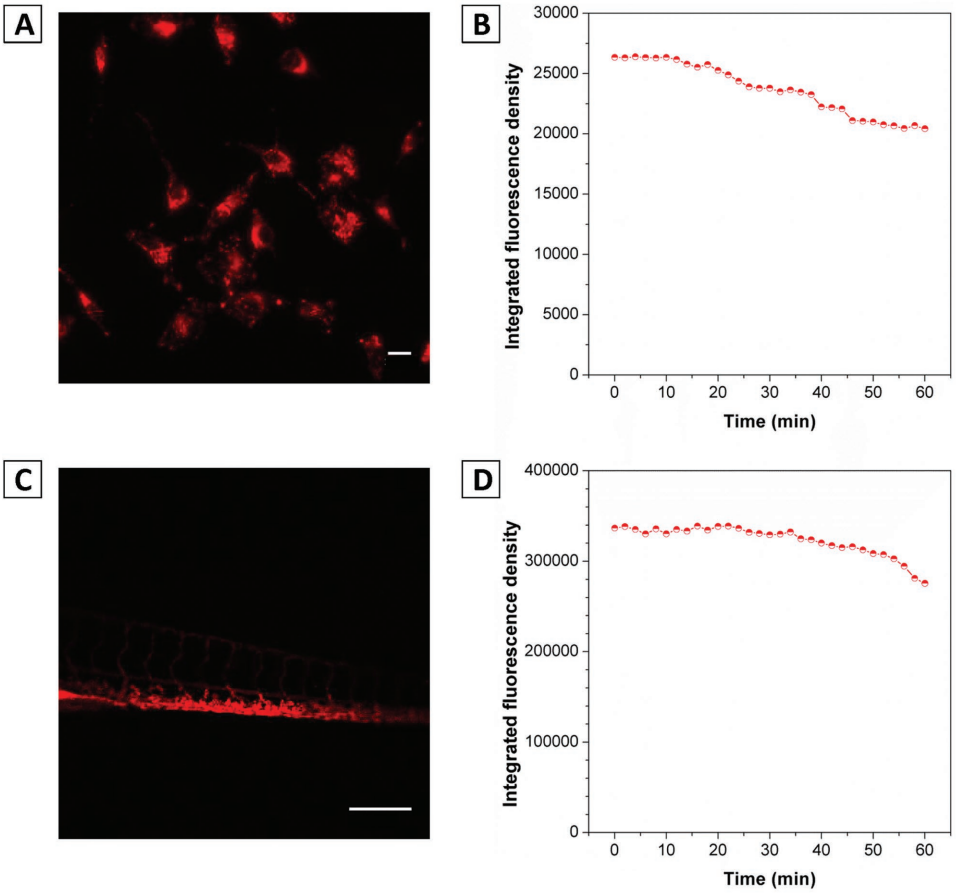

Figure 9. Photostability assay of *t*-BPITBT-TPE in NH_2-TAT NPs in A,B) HeLa cells and C,D) zebrafish larvae under continuous confocal laser scanning at 488 nm excitation. Scale in (A) depicts 20 μm and scale in (C) depicts 200 μm.

the contrary, the NH_2-TAT NPs in the trunk region show localization in the caudal hematopoietic tissue and caudal vein tissue near the tail (Figure 8B). This is due to the quicker uptake of the NPs in circulation, offering them less time to penetrate through the vasculature. The NH_2-TAT NPs can hence be used to ensure a quicker uptake in tissue around the vasculature, owing to its positive charges.

The excellent biocompatibility of the NH_2-TAT NPs and the effective cell uptake in zebrafish larvae inspired us to apply them for xenotransplantation of cancer cell lines to assess its potential as a quantitative long term cell tracker that gauge metastatic potential from different cancer cells. The photostability of the NPs was assessed in vitro and in vivo by subjecting HeLa cells and zebrafish larvae tagged with *t*-BPITBT-TPE in NH_2-TAT NPs to continuous laser ablation for 60 min. The fluorescent signals in vitro and in vivo were found to be stable (**Figure 9**), indicating excellent photostability of the NPs.

Two cell lines of different proliferative and metastatic phenotype, HeLa and MCF-7, were selected for the study. HeLa cells are known to possess aggressive tumorigenic properties while MCF-7 cells are known to be relatively mild in their behavior.[26] The cellular uptake and cytotoxicity evaluation results are shown in **Figure 10**. The confocal images show significant internalization of the NH_2-TAT NPs into the cytoplasm of the cells to give bright red fluorescence. Cell tracking was performed for both stained cell lines for 5 d in order to confirm the presence of fluorescent signal after multiple cell division cycles. As illustrated in Figure S6 (Supporting Information), the cells were found to still fluoresce up until the fifth day, indicating the good long-term tracing ability of these NPs. The MTT assay was performed to evaluate the toxicity of the NPs to the HeLa and MCF-7 cells and was found to be of low toxicity even up to 60 μg mL^{-1} based on *t*-BPITBT-TPE concentration.

The stained HeLa and MCF-7 cells were xenografted into the yolk sac of zebrafish larvae (1 dpf) to track in vivo cancer cell growth over time. The yolk sac is considered to be the optimal site for transplantation since it is nutrient rich and acellular.[27] The HeLa cells stained with *t*-BPITBT-TPE NPs (30 μg mL^{-1}) were suspended in a solution containing polyvinylpyrrolidone and fetal bovine serum (3×10^6 cells mL^{-1}) and microinjected into zebrafish larvae. Each successfully xenotransplanted zebrafish was individually tracked for five days to trace the dye integrity over multiple cancer cell proliferations and analyze the metastasis potential of injected cells in vivo.

To compare the behaviors of two different cancer cell lines, grafts of identical size were selected. The grafts selected were of small size (50–100 cells) so that the metastatic phenotype could be captured. In **Figure 11**A, individually tracked zebrafish xenografted with HeLa cells shows cancer cell proliferation and metastasis at 5 d post transplantation. In comparison, MCF-7

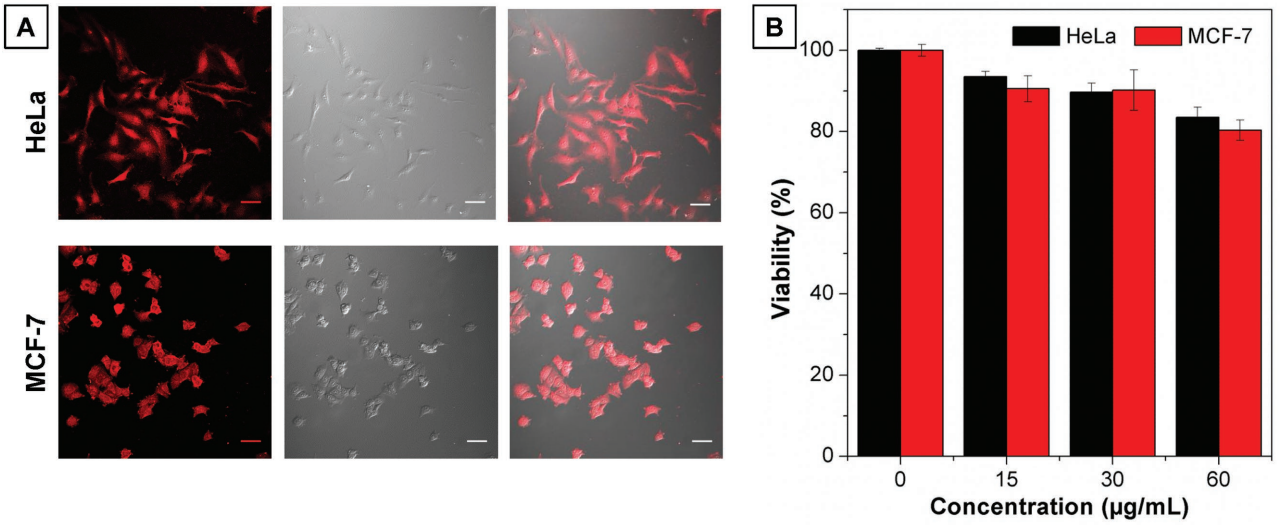

Figure 10. A) Confocal images of HeLa and MCF-7 cells stained with 30 μg mL^{-1} of NH_2-TAT NPs based on *t*-BPITBT-TPE concentration. The scale bar is 50 μm. B) MTT assay depicting the viability of HeLa and MCF-7 cells stained with different concentrations of NH_2-TAT NPs.

cancer cells do not proliferate as aggressively. Metastasis of the cells from the site of injection occurs through transport routes like the circulation network[28] and hence is analogous to the cancer cell metastasis in human. The HeLa cells are capable of detaching from the tumor and migrating through the circulation down to the caudal vasculature as seen in Figure 11B.

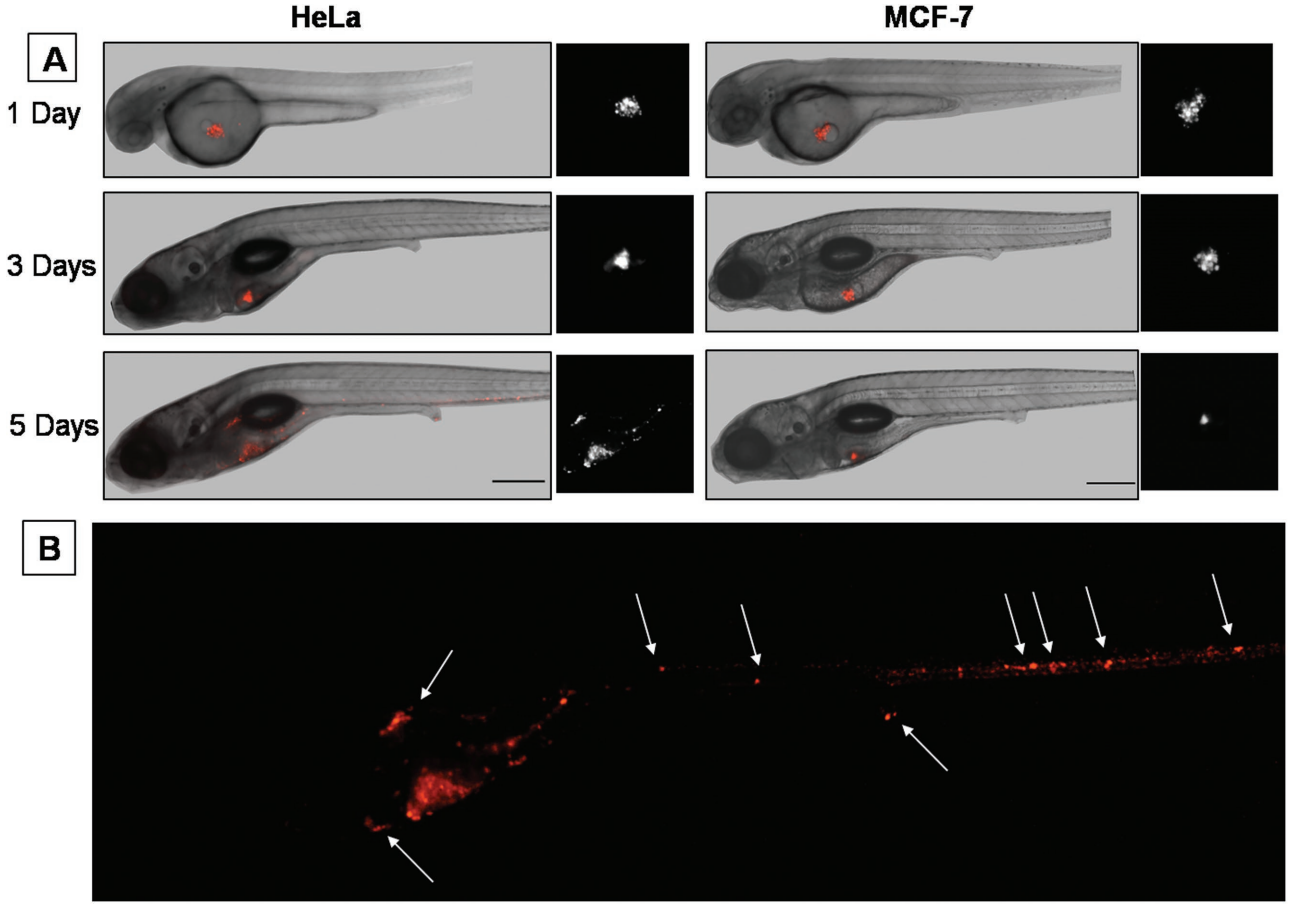

Figure 11. A) Tumor graft progression over 5 d in zebrafish larvae xenografted with fluorescent HeLa and MCF-7 cells; inset showing grayscale images of cancer cells. B) Fluorescent image of HeLa cell migration post dissemination. The scale bar is 200 μm.

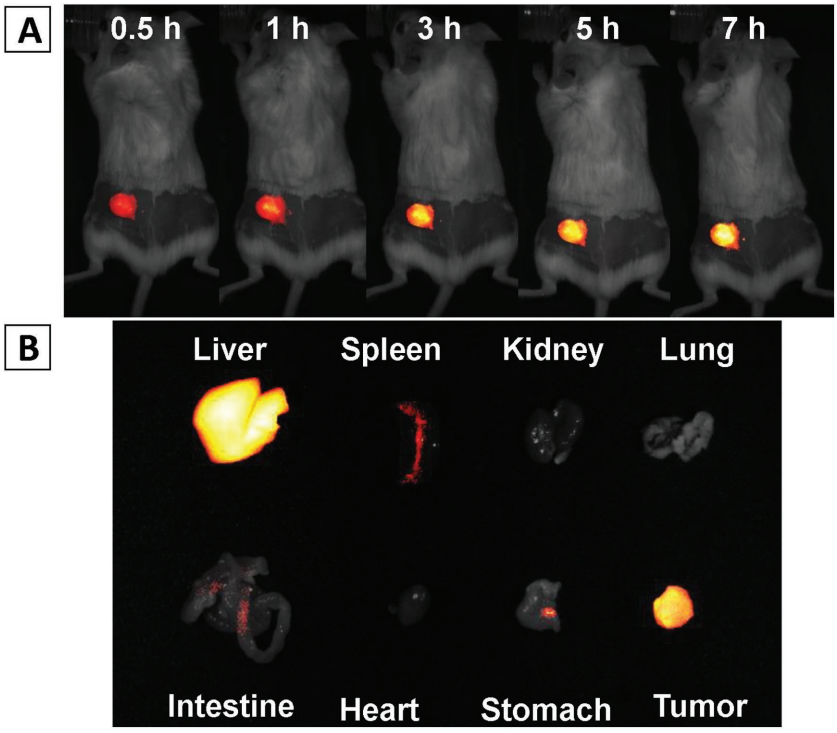

Figure 12. A) Accumulation of *t*-BPITBT NH_2-TAT NPs in tumor xenograft at different time postintravenous injection, and B) distribution of the NPs in different organ tissues.

No such metastatic behavior was observed in zebrafish larvae xenografted with MCF-7 cells (Figure S7, Supporting Information). These results reveal that the NH_2-TAT NPs enable the quantitative tracking of dynamic cancer cell proliferation and metastasis.

To demonstrate that *t*-BPITBT-TPE NPs are also suitable for mice imaging, BALB/c mice xenografted with 4T1 tumors were injected with 1 mg mL^{-1} of NH_2-TAT NPs intravenously. The results showed that the NPs accumulated in the tumor over a period of 7 h, and the fluorescent signals in the tumor gradually intensified over time and achieved the highest brightness at 7 h postintravenous injection of NPs (**Figure 12**A), demonstrating good in vivo imaging ability of NH_2-TAT NPs toward 4T1 tumors. The mice were sacrificed after 7 h and the NP distribution was investigated in the different organs, including heart, liver, spleen, kidney, lung, intestine, and stomach, resected and imaged immediately using a Maestro optical imaging system. As displayed in Figure 12B, the NPs flowed in the circulatory system of mice, and predominantly accumulated in liver, which was ascribed to the metabolic function of animals.

3. Conclusion

In summary, robust red fluorophores BPITBT-TPE and *t*-BPITBT-TPE with high solid-state fluorescence efficiencies were designed and synthesized. The introduction of AIE-active TPE could effectively alleviate the emission quenching of the molecules with electronic D–A structures in the aggregated state. In addition, solid-state fluorescence efficiency modulation was readily realized just by a *tert*-butyl group, which had been found to apparently impact the molecular arrangement in the crystalline state. A detailed toxicity and biodistribution profile in the zebrafish model was established for *t*-BPITBT-TPE-based NPs with different encapsulating matrices. The NPs with highly negative surface charges were found to be significantly toxic to the zebrafish embryos through transdermal permeation. As the surface charge increased to more positive, the toxicity decreased. The NP formulations with least toxicity were chosen to be injected into the zebrafish larvae intravenously. Through this delivery method, the long term toxicity and uptake of the NPs was evaluated. The difference in uptake from the vasculature and ability to penetrate tissue of positively and negatively charged NPs was demonstrated. The NPs decorated with TAT peptide showed efficient cellular uptake and were used to stain HeLa and MCF-7 cells which were xenografted in zebrafish. The NH_2-TAT NPs enabled long term tracing of the proliferation and metastasis of HeLa and MCF-7 cells in zebrafish. Since a large number of zebrafish embryos can be transplanted with biocompatible fluorescent NP tagged cancer cells, the same strategy can further be used in zebrafish model for drug screening. In addition, NH_2-TAT NPs also showed good imaging ability toward 4T1 tumors in xenografted mice. These results demonstrate that organic nanoparticles with strong red fluorescence and various functional groups on surface could be promising contrast reagents for biological applications.

4. Experimental Section

Synthesis of 4-(5-(1-(4-(Tert-Butyl)Phenyl)-1H-Phenanthro[9,10-d]Imidazol-2-yl)Thiophen-2-yl)-7-(4-(1,2,2-Triphenylvinyl)Phenyl)-Benzo[c][1,2,5]Thiadiazole (t-BPITBT-TPE): Into a mixture of **4b** (563 mg, 1.1 mmol), **5** (411 mg, 1.0 mmol), **6** (388 mg, 1.0 mmol), $Pd(PPh_3)_4$ (70 mg, 0.06 mmol), and Na_2CO_3 (530 mg, 5.0 mmol), 40 mL of THF and 10 mL of deionized water were added. The reaction mixture was stirred and refluxed for 18 h under nitrogen atmosphere. After cooling to room temperature, the mixture was poured into water and extracted with dichloromethane for three times. Before solvent evaporation, the combined organic extracts were dried over anhydrous magnesium sulfate. The crude product was purified by silica-gel column chromatography using petroleum ether/dichloromethane as eluent. *t*-BPITBT-TPE was obtained as red solid in 22% yield (142 mg). ^{1}H NMR (500 MHz, CD_2Cl_2), δ (ppm): 8.91 (d, J = 7.6 Hz, 1H), 8.72 (dd, J = 20.5, 8.3 Hz, 2H), 7.91 (d, J = 4.1 Hz, 1H), 7.88 (d, J = 7.5 Hz, 1H), 7.81–7.76 (m, 5H), 7.69–7.66 (m, 2H), 7.63–7.60 (m, 2H), 7.53–7.50 (m, 1H), 7.30–7.26 (m, 1H), 7.23–7.10 (m, 16H), 7.07–7.03 (m, 3H), 1.54 (s, 9H). ^{13}C NMR (126 MHz, CD_2Cl_2), δ (ppm): 155.01, 154.14, 153.00, 146.06, 144.40, 144.17, 144.13, 144.11, 141.96, 141.36, 140.90, 135.75, 135.50, 132.86, 131.81, 131.70, 131.63, 131.59, 129.50, 128.98, 128.81, 128.71, 128.23, 128.14, 128.04, 127.75, 127.02, 126.93, 126.87, 126.18, 126.12, 125.83, 125.51, 124.39, 123.58, 123.19, 121.18, 35.53, 31.66.

HRMS ($C_{61}H_{44}N_4S_2$): *m/z* 896.3014 [M^+, calcd 896.3007]. Anal. Calcd for $C_{61}H_{44}N_4S_2$: C, 81.66; H, 4.94; N, 6.24. Found: C, 81.55; H, 5.10; N, 6.15%.

The synthetic procedure to PITBT-TPE was analogous to that of *t*-BPITBT-TPE. Red solid, yield 18%. ^{1}H NMR (500 MHz, CD_2Cl_2), δ (TMS, ppm): 9.02 (br, 1H), 8.81 (d, 1H, J = 9.0 Hz), 8.77 (d, 1H, J = 8.5 Hz), 7.99–7.95 (m, 2H), 7.89–7.83 (m, 6H), 7.77–7.75 (m, 4H), 7.60–7.57 (m, 1H), 7.34–7.31 (m, 1H), 7.25–7.10 (m, 19H). The ^{13}C NMR data are not available due to its limited solubility in common deuterated solvents, such as $CDCl_3$ and CD_2Cl_2. HRMS ($C_{57}H_{36}N_4S_2$): *m/z* 840.2393 (M^+, calcd 840.2381). Anal. Calcd for $C_{57}H_{36}N_4S_2$: C, 81.40; H, 4.31; N, 6.66. Found: C, 80.97; H, 4.34; N, 6.57%.

Crystal Data for t-BPITBT-TPE (CCDC 1502964): $C_{61}H_{44}N_4S_2{\cdot}CH_2Cl_2$, M_W = 982.05, triclinic, P-1, a = 12.9771(7) Å, b = 12.9950(8) Å, c = 16.5755(9) Å, α = 98.365(2)°, β = 100.440(2)°, γ = 111.832(2)°, V = 2481.5(2) Å^{-3}, Z = 2, D_c = 1.314 g cm^{-3}, μ = 0.261 mm^{-1} (MoKα, λ = 0.71073), F(000) = 1024, T = 173(2) K, $2\theta_{max}$ = 25.38° (98.0%), 22615 measured reflections, 8943 independent reflections (R_{int} = 0.0709), goodness of fit (GOF) on F^2 = 1.027, R_1 = 0.1208, wR_2 = 0.1283 (all data), Δe 0.290 and –0.418 eÅ^{-3}.

Crystal Data for PITBT-TPE (CCDC 1502965): $C_{57}H_{36}N_4S_2{\cdot}2(CH_2Cl_2)$, M_W = 1010.87, monoclinic, $P2_1/n$, a = 11.8521(15) Å, b = 26.434(4) Å, c = 14.763(2) Å, β = 91.886(6)°, V = 4622.9(11) Å^{-3}, Z = 4, D_c = 1.452 g cm^{-3}, μ = 0.394 mm^{-1} (MoKα, λ = 0.71073), F(000) = 2088, T = 173(2) K, $2\theta_{max}$ = 24.50° (99.1%), 28671 measured reflections, 7623 independent reflections (R_{int} = 0.0875), GOF on F^2 = 1.068, R_1 = 0.1194, wR_2 = 0.1930 (all data), Δe 0.651 and –0.976 eÅ^{-3}.

Nanoparticle Preparation: The organic NPs were prepared by nanoprecipitation. 200 µL DSPE-PEG_{2000} (—OCH_3, —COOH, or —NH_2) in THF at 4 mg mL^{-1} was mixed with 800 µL of *t*-BPITBT-TPE in THF at 2 mg mL^{-1} to yield a 1 mL solution. The organic solution was injected rapidly into 10 mL of water under probe sonication at 12 W to ensure maximum agitation. The solution was stirred overnight to ensure evaporation of the THF. The solution was then filtered through a 220 nm syringe filter and concentrated to 640 µg mL^{-1} stock using a centrifuge filter.

The NH_2-TAT NPs were prepared by mixing 100 µL of DSPE-PEG_{2000}-NH_2, 100 µL of DSPE-PEG_{2000}-maleimide at 4 mg mL^{-1} in THF and 800 µL of *t*-BPITBT-TPE in THF at 2 mg mL^{-1} to yield a 1 mL solution. The organic solution was injected rapidly into 10 mL of water under probe sonication at 12 W to ensure maximum agitation. The 10 mL stock after syringe filtration was stirred with a solution of TAT peptide in DMSO (10 mg mL^{-1}) for 24 h followed by dialysis (10 kDa MWCO) for 3 d to ensure complete DMSO removal. The stock was then concentrated using a centrifuge filter.

Zebrafish Line and Toxicity Test: Four to five pairs of zebrafish were placed in crossing tanks for spawning overnight. Embryos were settled to the bottom of the tank, and were collected using a sieve and transferred to petri dishes for embryo culture. They were screened, incubated at 27 °C, 0.4% CO_2 and grown in egg water (10% NaCl; 1.63% $MgSO_4{\cdot}7H_2O$; 0.4% $CaCl_2$; 0.3% KCl). After 22 h postfertilization, PTU was added to prevent melanin formation to yield optically transparent fish. 3 d postfertilization the embryos were seeded to into 96 well plates at 1 embryo per well. The embryos were soaked in 100 µL of NPs at various concentrations for 24 h and were imaged for uptake using confocal imaging (Carl Zeiss LSM 510 Meta) using 488 nm.

Microinjection: Local in vivo injection of the NPs intravenously was done using a nitrogen gas injector. The needle used for injection is made by pulling glass capillary tubes (O.D. 1.0 mm, I.D. 0.75 mm) in a needle puller which heats to pull the glass tubes into fine needles (20 µm). The NPs were filled into the needles which were loaded into the nitrogen gas injector. The injector was operated in continuous mode for the retro-orbital delivery of the NPs. The fishes were mounted in a mixture of 1% low melting agarose and 5% methyl cellulose for the injection and confocal imaging.

HeLa and MCF-7 Cell Imaging and Toxicity Analysis: HeLa and MCF-7 cells were cultured at 37 °C and 5% CO_2 in Dulbecco's Modified Eagle Medium (DMEM). After reaching 70% confluence, the culture medium was removed. Then the adherent cells were washed with 1× phosphate buffered saline (PBS) buffer twice. The NH_2-TAT NPs in DMEM at a concentration 30 µg mL^{-1} (based on *t*-BPITBT-TPE mass concentration) were added into the well plate. After 2 h of incubation, the cells were washed with 1× PBS buffer three times and following were fixed with 75% ethanol for 20 min. The cells were further washed with 1× PBS buffer two times. The cells were then mounted and studied with confocal laser scanning microscope (Zeiss LSM 800, Jena, Germany).

The toxicity of NH_2-TAT NPs to HeLa and MCF-7 cells was characterized with MTT assay. HeLa and MCF-7 cells were cultured for 24 h in the 96 well plates (Costar, IL, USA) at a density of 5×10^4 cells mL^{-1}. Different concentrations of NPs suspension were used to replace the cell medium. The cells were cultured for another 4 h. Subsequently, 10 µL of freshly prepared MTT solution with a concentration of 5 mg mL^{-1} was added into each well. Post 3 h of incubation, MTT medium solution was removed. 100 µL of DMSO was added into each well to dissolve the formed precipitates. A microplate reader (Genios Tecan) was used to monitor the absorbance at 570 nm of MTT. The cell viability was calculated by the ratio of the absolute absorbance of the cells treated with NPs suspension to that of the cells only cultured in culture medium.

HeLa and MCF-7 Cell Preparation and Xenotransplantation: HeLa and MCF-7 cells were stained with *t*-BPITBT-TPE NPs encapsulated in DSPE-PEG-NH_2-TAT matrix. Cells were cultured with DMEM at 37 °C in a humidified environment with 5% CO_2. The DMEM media contained 10% of fetal bovine serum and 1% of penicillin streptomycin. Before experiments, the cells were precultured until confluence was reached. The cells were treated with 30 µg mL^{-1} of *t*-BPITBT-TPE NPs in DMEM media for 2 h. Subsequently, the adherent cells were washed with 1× PBS buffer twice, trypsinized and resuspended in media. The cells were transferred to 1.5 mL Eppendorf tubes and centrifuged 5 min, at 1500 rpm. Cells were resuspended in 0.5 mL of solution containing 2.5% polyvinylpyrrolidone (PVP-40) in fetal calf serum to obtain a concentration of 3×10^6 cells mL^{-1}. 1 dpf zebrafish embryos were dechorionated and immobilized by mounting in a mixture 1% low melting agarose and 5% methyl cellulose. Using a manual injector (Harvard apparatus), the cell suspension was loaded into an injection needle (O.D. 1.0 mm, I.D. 0.75 mm). Cells were now injected in 1 dpf wild type zebrafish embryos. After injection, embryos were incubated for 1 h at 25 °C and checked for cell presence. All other fish were incubated at 32.5 °C for the following days and imaged using Carl Zeiss LSM 510 Meta microscope.

Fluorescence Imaging in Xenografted Mice: 4T1 cancer cells (1×10^6) suspended in 30 µL of saline were injected subcutaneously into the left back of the BALB/c mice. Tumors were grown until a single aspect was ≈7 mm (approximately two weeks) before fluorescence imaging. BALB/c mice bearing 4T1 tumors were intravenously injected with *t*-BPITBT-TPE NH_2-TAT NPs (100 µL, 1 mg mL^{-1}) (n = 5), respectively. Fluorescence signals were captured after NPs administration. 7 h after NP injection, mice were sacrificed and different tissues were collected, imaged by the Maestro system.

Supporting Information

Supporting Information is available from the Wiley Online Library or from the author.

Acknowledgements

G.L. and P.N.M. contributed equally to this work. The authors acknowledge the financial support from the National Natural Science Foundation of China (21673082), the Guangdong Natural Science Funds for Distinguished Young Scholar (2014A030306035), the Fundamental Research Funds for the Central Universities (2017ZD001 and 2015ZY013), NRF Investigatorship (R279-000-444-281), National University of Singapore (R279-000-482-133), the Natural Science Foundation of

Guangdong Province (2016A030312002), and the Innovation and Technology Commission of Hong Kong (ITC-CNERC14SC01).

Conflict of Interest

The authors declare no conflict of interest.

Keywords

aggregation-induced emission, cancer cell progression, fluorescence imaging, nanoparticles, zebrafish

Received: March 17, 2017
Revised: May 4, 2017
Published online:

[1] a) L. Yuan, W. Lin, K. Zheng, L. He, W. Huang, *Chem. Soc. Rev.* **2013**, *42*, 622; b) H. Kobayashi, M. Ogawa, R. Alford, P. L. Choyke, Y. Urano, *Chem. Rev.* **2010**, *110*, 2620; c) J. Mérian, J. Gravier, F. Navarro, I. Texier, *Molecules* **2012**, *17*, 5564; d) Q. Hu, M. Gao, G. Feng, B. Liu, *Angew. Chem., Int. Ed.* **2014**, *53*, 14225; e) Y. Yuan, R. T. K. Kwok, B. Z. Tang, B. Liu, *J. Am. Chem. Soc.* **2014**, *136*, 2546.

[2] P. Das, N. R. Jana, *ACS Appl. Mater. Interfaces* **2014**, *6*, 4301.

[3] a) K. Li, W. Qin, D. Ding, N. Tomczak, J. Geng, R. Liu, J. Liu, X. Zhang, H. Liu, B. Liu, B. Z. Tang, *Sci. Rep.* **2013**, *3*, 1150; b) S. Chen, H. Wang, Y. Hong, B. Z. Tang, *Mater. Horiz.* **2016**, *3*, 283; c) A. Reisch, A. S. Klymchenko, *Small* **2016**, *12*, 1968; d) H.-S. Peng, D. T. Chiu, *Chem. Soc. Rev.* **2015**, *44*, 4699.

[4] D. M. Shcherbakova, O. M. Subach, V. V. Verkhusha, *Angew. Chem., Int. Ed.* **2012**, *51*, 10724.

[5] J. Geng, K. Li, W. Qin, L. Ma, G. G. Gurzadyan, B. Z. Tang, B. Liu, *Small* **2013**, *9*, 2012.

[6] a) Y. Li, A. Shao, Y. Wang, J. Mei, D. Niu, J. Gu, P. Shi, W. Zhu, H. Tian, J. Shi, *Adv. Mater.* **2016**, *28*, 3187; b) L. Yan, Y. Zhang, B. Xu, W. Tian, *Nanoscale* **2016**, *8*, 2471.

[7] a) K. Zheng, W. Lin, W. Huang, X. Guan, D. Cheng, J.-Y. Wang, *J. Mater. Chem. B* **2015**, *3*, 871; b) Q. Zhao, K. Li, S. Chen, A. Qin, D. Ding, S. Zhang, Y. Liu, B. Liu, J. Z. Sun, B. Z. Tang, *J. Mater. Chem.* **2012**, *22*, 15128.

[8] a) X. Han, Q. Bai, L. Yao, H. Liu, Y. Gao, J. Li, L. Liu, Y. Liu, X. Li, P. Lu, B. Yang, *Adv. Funct. Mater.* **2015**, *25*, 7521; b) Z. Zhao, J. Geng, Z. Chang, S. Chen, C. Deng, T. Jiang, W. Qin, J. W. Y. Lam, H. S. Kwok, H. Qiu, B. Liu, B. Z. Tang, *J. Mater. Chem.* **2012**, *22*, 11018; c) L. Yao, S. Zhang, R. Wang, W. Li, F. Shen, B. Yang, Y. Ma, *Angew. Chem., Int. Ed.* **2014**, *53*, 2119.

[9] a) J. Mei, N. L. C. Leung, R. T. K. Kwok, J. W. Y. Lam, B. Z. Tang, *Chem. Rev.* **2015**, *115*, 11718; b) J. Mei, Y. Hong, J. W. Y. Lam, A. Qin, Y. Tang, B. Z. Tang, *Adv. Mater.* **2014**, *26*, 5429; c) Y. Hong, J. W. Y. Lam, B. Z. Tang, *Chem. Soc. Rev.* **2011**, *40*, 5361.

[10] a) H. Lu, Y. Zheng, X. Zhao, L. Wang, S. Ma, X. Han, B. Xu, W. Tian, H. Gao, *Angew. Chem., Int. Ed.* **2016**, *55*, 155; b) M. Chen, L. Li, H. Nie, J. Tong, L. Yan, B. Xu, J. Z. Sun, W. Tian, Z. Zhao, A. Qin, B. Z. Tang, *Chem. Sci.* **2015**, *6*, 1932.

[11] a) Y. Zhao, C. Shi, X. Yang, B. Shen, Y. Sun, Y. Chen, X. Xu, H. Sun, K. Yu, B. Yang, Q. Lin, *ACS Nano* **2016**, *10*, 5856; b) D. Ding, R. T. K. Kwok, Y. Yuan, G. Feng, B. Z. Tang, B. Liu, *Mater. Horiz.* **2015**, *2*, 100; c) Y. Yuan, C.-J. Zhang, M. Gao, R. Zhang, B. Z. Tang, B. Liu, *Angew. Chem., Int. Ed.* **2015**, *54*, 1780; d) Y. Huang, F. Hu, R. Zhao, G. Zhang, H. Yang, D. Zhang, *Chem. Eur. J.* **2014**, *20*, 158; e) Y. Yuan, S. Xu, X. Cheng, X. Cai, B. Liu, *Angew. Chem., Int. Ed.* **2016**, *55*, 6457.

[12] a) S. Lin, Y. Zhao, A. E. Nel, S. Lin, *Small* **2013**, *9*, 1608; b) J.-W. Fan, R. Vankayala, C.-L. Chang, C.-H. Chang, C.-S. Chiang, K. C. Hwang, *Nanotechnology* **2015**, *26*, 215703; c) Z. He, Y. Sun, J. Cao, Y. Duan, *Phys. Chem. Chem. Phys.* **2016**, *18*, 11986; d) D. Li, X. Zhao, W. Qin, H. Zhang, Y. Fei, L. Liu, K.-T. Yong, G. Chen, B. Z. Tang, J. Qian, *Nano Res.* **2016**, *9*, 1921.

[13] A. Amsterdam, R. M. Nissen, Z. Sun, E. C. Swindell, S. Farrington, N. Hopkins, *Proc. Natl. Acad. Sci. USA* **2004**, *101*, 12792.

[14] S.-K. Ko, X. Chen, J. Yoon, I. Shin, *Chem. Soc. Rev.* **2011**, *40*, 2120.

[15] F. Progatzky, M. J. Dallman, C. Lo Celso, *Interface Focus* **2013**, *3*, 20130001.

[16] H. Feitsma, E. Cuppen, *Mol. Cancer Res.* **2008**, *6*, 685.

[17] a) X.-J. Yang, W. Cui, A. Gu, C. Xu, S.-C. Yu, T.-T. Li, Y.-H. Cui, X. Zhang, X.-W. Bian, *PLoS ONE* **2013**, *8*, e61801; b) I. J. Marques, F. U. Weiss, D. H. Vlecken, C. Nitsche, J. Bakkers, A. K. Lagendijk, L. I. Partecke, C.-D. Heidecke, M. M. Lerch, C. P. Bagowski, *BMC Cancer* **2009**, *9*, 1.

[18] A. M. Taylor, L. I. Zon, *Zebrafish* **2009**, *6*, 339.

[19] S. H. Lam, H. L. Chua, Z. Gong, T. J. Lam, Y. M. Sin, *Dev. Comp. Immunol.* **2004**, *28*, 9.

[20] J. Tat, M. Liu, X.-Y. Wen, *Drug Discovery Today Technol.* **2013**, *10*, e83.

[21] Y. Zhang, J.-H. Wang, J. Zheng, D. Li, *Chem. Commun.* **2015**, *51*, 6350.

[22] Z. Zhao, S. Chen, J. W. Y. Lam, C. K. W. Jim, C. Y. K. Chan, Z. Wang, P. Lu, C. Deng, H. S. Kwok, Y. Ma, B. Z. Tang, *J. Phys. Chem. C* **2010**, *114*, 7963.

[23] J. Xiang, X. Cai, X. Lou, G. Feng, X. Min, W. Luo, B. He, C. C. Goh, L. G. Ng, J. Zhou, Z. Zhao, B. Liu, B. Z. Tang, *ACS Appl. Mater. Interfaces* **2015**, *7*, 14965.

[24] T. A. Kelf, V. K. A. Sreenivasan, J. Sun, E. J. Kim, E. M. Goldys, A. V. Zvyagin, *Nanotechnology* **2010**, *21*, 285105.

[25] S. Honary, F. Zahir, *Trop. J. Pharm. Res.* **2013**, *12*, 255.

[26] E. Iorns, K. Drews-Elger, T. M. Ward, S. Dean, J. Clarke, D. Berry, D. E. Ashry, M. Lippman, *PLoS ONE* **2012**, *7*, e47995.

[27] C. J. Veinotte, G. Dellaire, J. N. Berman, *Dis. Model. Mech.* **2014**, *7*, 745.

[28] M. Konantz, T. B. Balci, U. F. Hartwig, G. Dellaire, M. C. André, J. N. Berman, C. Lengerke, *Ann. N. Y. Acad. Sci.* **2012**, *1266*, 124.